PCCP

ROYAL SOCIETY OF CHEMISTRY

PAPER

View Article Online
View Journal | View Issue

Cite this: *Phys. Chem. Chem. Phys.*, 2022, **24**, 4065

Temperature-dependent excitonic emission characteristics of lead-free inorganic double perovskites and their third-order optical nonlinearities†

Avanendra Singh,*[a] Pritam Dey,[a] Anupa Kumari,[b] Mrinal Kanti Sikdar,[b] Pratap K. Sahoo,[b] Ritwick Das[b] and Tanmoy Maiti*[a]

Received 26th October 2021,
Accepted 16th January 2022

DOI: 10.1039/d1cp04896a

rsc.li/pccp

We report temperature-dependent photoluminescence (PL) in the temperature range between 77 K and 300 K, and room temperature nonlinear optical (NLO) properties of solution processed lead-free Cs_2NaBiI_6 (CNBI) and Cs_2KBiI_6 (CKBI) perovskite films. The de-convolution analysis of temperature-dependent PL spectra showed thermal quenching behavior of free-exciton (FX) emission, an unusual blue-shift of PL emission, and line broadening with increasing temperature as a consequence of strong exciton–phonon interaction. The nonlinear refractive index (n_2) and nonlinear absorption coefficient (β) of both the CNBI and CKBI films are determined using a closed aperture (CA) and open aperture (OA) Z-scan technique, respectively. Both the CNBI and CKBI perovskites exhibited features of saturable absorption (SA) with $\beta \sim -6.23 \times 10^{-12}$ cm W^{-1}, and -1.14×10^{-12} cm W^{-1}, respectively. The CA measurements depicted a self-defocusing effect in both the samples with n_2 values $\sim -1.06 \times 10^{-14}$ cm^2 W^{-1} and -1.337×10^{-14} cm^2 W^{-1}, respectively. With such emission and NLO characteristics, CNBI and CKBI perovskite films can be used for designing eco-friendly optoelectronic and NLO devices.

Introduction

In recent years, organic–inorganic hybrid halide perovskites have gained wide attention for designing efficient optoelectronic and optical devices including light emitting diodes (LEDs),[1] nonlinear optical switches and lasers *etc.*,[2] owing to their excellent absorption characteristics in the visible region, long-carrier diffusion lengths, low trap state densities,[3] small exciton binding energies,[1] and high nonlinear absorption coefficients.[4,5] In the literature, recently some efforts have been made to improve the performance of LEDs.[6] With this aim, Xiao *et al.*[7] have reported ~10% efficiency in nanometre-sized crystallites of perovskites, Xu *et al.* achieved ~21.6% efficiency by weakening the bonding between the passivating functional moieties and the organic cations,[8] Matsushima *et al.* achieved ~30% efficiency by incorporating perovskite transport layers with high carrier mobilities into OLEDs with high color purity.[9] Also, these perovskites are known to exhibit a high solar cell efficiency exceeding ~20%.[10,11] In spite of the improved device efficiencies of lead–halide based organometallic perovskites, these materials suffer from durability issues with respect to moisture and heat, which hinders their utilization for large scale industrial integration. In order to develop alternative routes to improve the stability of perovskite materials, recently attempts have been made to synthesize inorganic perovskites.[12–14] Among the various inorganic halide perovskites reported in the literature, caesium based inorganic lead halide perovskite quantum dots (QDs) exhibit narrow emission line widths, quite bright and tunable emission profiles along with a very high quantum yield[15–17] with no requirement for a surface passivation layer due to their high defect tolerance.[18] Apart from the promising optoelectronic properties, $CsPbBr_3$ perovskites have also shown low lasing thresholds ($\tau \sim 4$ μJ cm^{-2}),[19] a high-quality factor, ($Q \sim 2256$)[20] and non-linear optical (NLO) behavior[21] with two-photon absorption (TPA)/multi-photon absorption characteristics.[22–24] With such extraordinary features, caesium based perovskites have been posited as an alternative to organic–inorganic hybrid perovskites for designing potential optoelectronic and non-linear optical devices. However, the presence of lead in $CsPbX_3$ perovskite hinders its application for a wide range of eco-friendly practical purposes, as lead is toxic and PbI_2 is carcinogenic. In this context, synthesis of stable lead-free inorganic perovskites with outstanding NLO characteristics along with a deep understanding of their fundamental photo-physical

[a] *Plasmonics and Perovskites Laboratory (PPL), Department of Materials Science and Engineering, Indian Institute of Technology, Kanpur, UP, India. E-mail: avanendr@iitk.ac.in, tmaiti@iitk.ac.in; Tel: +91 (0512) 2596994*

[b] *School of Physical Sciences, National Institute of Science Education and Research, HBNI, Bhubaneswar, Odisha, India*

† Electronic supplementary information (ESI) available. See DOI: 10.1039/d1cp04896a

properties is required. In the search for an alternative to the toxic and poor open environment stability of lead-based organic perovskites, bismuth based perovskites have been explored recently, owing to their better thermal and moisture stability.[25] By considering the outstanding optoelectronic characteristics of cesium based lead-halide perovskites, replacement of Pb by Bi with proper charge neutrality can combine the optoelectronic properties with improved thermal and moisture stability. Since the incorporation of Bi^{3+} into the lattice may also introduce vacancies, and can be minimized by incorporating a mono-valent alkali metal into the host lattice, thus giving a structure of double perovskite $A_2B_2X_6$ (X = I, Cl, Br).[26,27] In this work, we have synthesized two lead-free caesium based double perovskites namely, Cs_2NaBiI_6 (CNBI) and Cs_2KBiI_6 (CKBI), and investigated their photo-physical properties using temperature-dependent photoluminescence (PL) spectroscopy in the temperature range from 77 K to 300 K, NLO characteristics *i.e.* a nonlinear refractive index coefficient (n_2) and absorption coefficient (β) using a single beam Z-scan technique in ambient conditions. The temperature-dependent PL study includes investigation of exciton dynamics through changes in PL intensity, spectral shift and line width.

The Z-scan measurements of both the perovskite films exhibit appreciably high NLO ($\chi^{(3)}$) characteristics at moderate power levels. These films exhibit a self-defocusing effect in closed aperture (CA) configuration and saturable absorption (SA) behaviour in open aperture (OA) configuration. With the observed promising emission, and NLO characteristics, the eco-friendly and stable CNBI and CKBI perovskite films could be an alternative for optoelectronic applications.

Experimental specification

Materials

Cesium iodide (99.999%), sodium iodide (NaI, 99.5%), potassium iodide (KI, 99%), bismuth iodide (BiI_3, 99.998%) and fluorine doped tin oxide (FTO) glass slides (13 Ω) were purchased from Sigma Aldrich India. Anhydrous γ-butyrolactone (GBL), toluene (AR), isopropyl alcohol (AR), and acetone (AR) were all purchased from Merck India. All the reagents except toluene were used without any further purification; toluene was distilled before use.

Synthesis of perovskite absorbers and film preparation

Although both CNBI and CKBI are brownish-red crystalline powders, CKBI appears to be darker. CNBI was synthesized by mixing a 2 : 1 : 1 equivalent molar ratio of cesium iodide, sodium iodide and bismuth iodide in 4 mL GBL inside a double-neck round-bottom flask (RBF).

$$2CsI + NaI + BiI_3 = Cs_2NaBiI_6 \quad (1)$$

$$2CsI + KI + BiI_3 = Cs_2KBiI_6 \quad (2)$$

The RBF was kept in a silicone oil bath for 4 h with continuous stirring and argon purging; the temperature of the solution was maintained at 100 °C. Furthermore, the final product was kept in a vacuum oven at 60 °C for 24 hours. The synthesis procedure for CKBI was the same as above. For spin coating of the films FTO coated glass substrates (20 mm × 20 mm) were cleaned in multi-steps; *i.e.* first, they were ultrasonicated with Hellmanex III soap solution (v/v = 2.5 : 100 in water) for 30 min under warm conditions followed by ultrasonication in isopropyl alcohol and a warm acetone–water mixture (v/v = 1 : 1) respectively for 15 min in each step. Before deposition, substrates were UVO_3 treated for 30 min. 0.44 M perovskite solution was prepared by dissolving GBL at 55 °C with simultaneous stirring for four hours. Spin coating (60 μL perovskite solution) was performed on preheated (100 °C) substrates at 2500 rpm for 30 seconds. Furthermore, 20 μL toluene (antisolvent) was swiftly sprayed on the perovskite film, just after 10 seconds of spin followed by annealing at 100 °C for 10 min. A schematic diagram of the film deposition is illustrated in Fig. 1.

Characterization

The crystal structure of both the perovskite films was investigated using an X-ray diffraction (XRD) technique in grazing incidence geometry. Room temperature absorption characteristics were studied using UV-visible spectroscopy, in which an un-polarized light incident on the sample at an incident angle of 45° with respect to the normal to the sample surface and the absorption spectra were recorded in the wavelength range from 400 nm to 800 nm. The emission behavior of both the samples was studied as a function of temperature using confocal temperature-dependent PL measurements in a temperature range from 77 K to 300 K. A 532 nm laser with spot size of ~1 μm was used as an excitation source, and PL spectra were recorded using a Peltier cooled CCD detector. NLO measurements were performed using a Z-scan technique, and a schematic of the experimental setup is shown in Fig. 2.[28]

A pulsed Yb-doped fiber laser (Model: Cazadero, M/S Calmar Inc., USA) is used as a pump source, which emits Fourier-transform

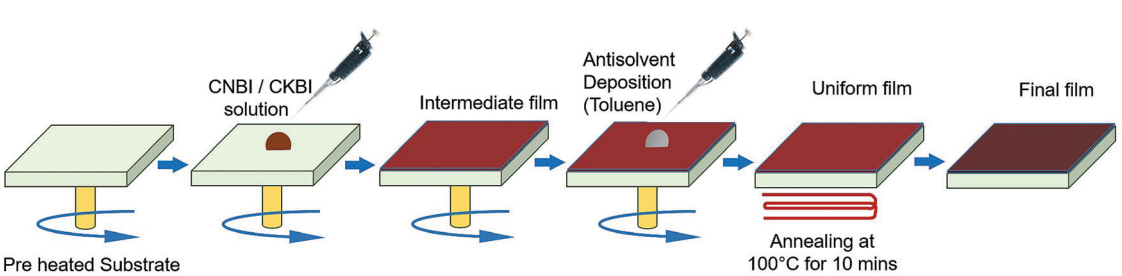

Fig. 1 Schematic diagram of a single step spin coating process with toluene treatment for CNBI/CKBI thin film coating.

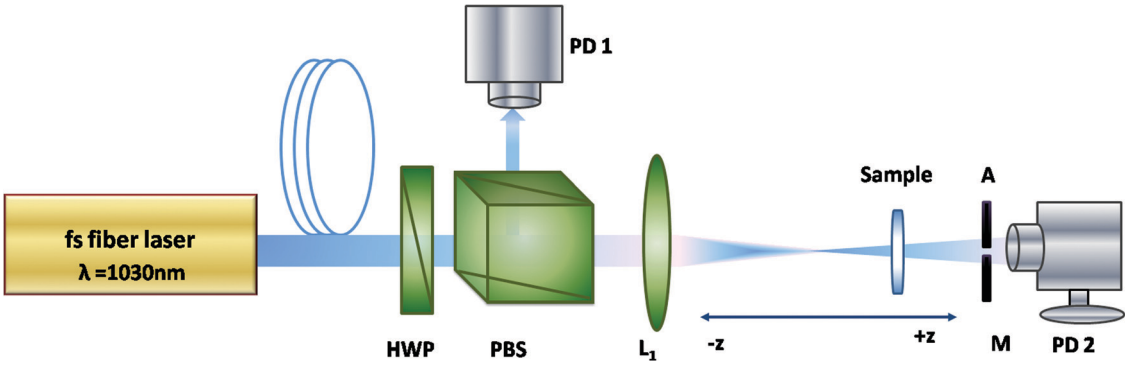

Fig. 2 Schematic diagram of the Z-scan experimental setup.

limited (FTL) ultra-short pulses ($\Delta\tau$ = 370 fs) at an operating wavelength of λ = 1030 nm. The Yb-fiber laser system delivers a fixed pulse energy of 30 μJ across a broad range of pulse repetition rates (RR), ranging from 780 Hz to 200 kHz. In our investigation, we fix the repetition rate at 1 kHz to minimize the thermally-induced effects during the NLO measurements. A combination of a half-wave plate (HWP) and a polarizing beam-splitter (PBS) is employed for incidence of optimum laser fluence on the samples. A convex lens (f = 150 mm) is used to focus the beam at the sample (z = 0). The beam spot-size at (z = 0) is measured to be ω_o = 52 μm which results in a Rayleigh-length of ~30 mm. Therefore, we could safely assume thin-sample approximation for estimating the NLO coefficients. Furthermore, we translate the sample to be about 110 mm in length which helps in acquiring sufficient information for obtaining normalized transmission. The CA as well as OA transmitted power were recorded using a photodiode sensor PD1 (model: PD3003W-V1, M/S Ophir Inc., USA).[29]

Results and discussion

In this work, we successfully synthesized two new halide based lead-free double perovskites, *i.e.* CNBI and CKBI, using the solution processing method. Fig. 3 shows a grazing angle XRD pattern of both the CNBI and CKBI thin films. As both the perovskites are newly synthesized, and not explored much, the literature lacks any standard JPDC card available for them. We have compared these XRD patterns with the already reported XRD pattern of CNBI powder,[30] consistent with a similar double perovskite, MA_2AgBiI_6.[31] The consistency of our XRD patterns with the reported data implies the formation of double perovskites of hexagonal crystal with the symmetric space group of $P6_3/mmc$.[32] In the XRD pattern of the CNBI sample, the peaks marked with a star symbol (*) are associated with the CNBI double perovskite peaks. Similarly, for CKBI, the Bragg peaks labeled with the Δ symbol are assigned to CKBI double perovskite peaks. In addition, peaks at ~21.1, 38.5, and 51.5° with low intensity are also observed in both the XRD patterns, which are formed by the decomposition of CNBI/CKBI into a secondary phase of $Cs_3Bi_2I_9$ (CBI).[30] In general, the CBI structure is formed by the partial decomposition of a double perovskite during the chemical process as temperature drops. The crystal

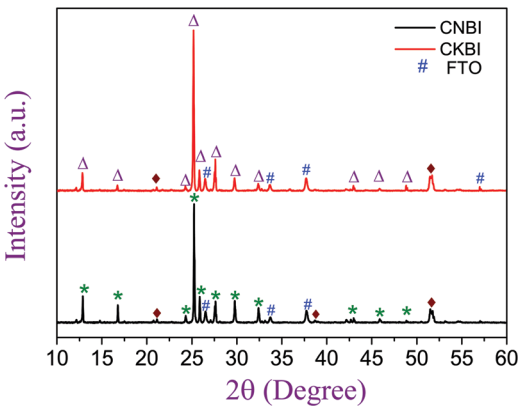

Fig. 3 X-Ray diffraction patterns of CNBI and CKBI thin films. The peaks marked with (#)originate from the FTO coated glass substrate.

structure of CBI is reported as a two-dimensional structure with two face-sharing metal–halide octahedra separated by cesium ions.[33] In Fig. S2 and S3 (ESI†), we observed that both the CNBI and CKBI perovskite films were stable for a duration of six months, without the emergence of any new peaks and no structural degradation. Fig. 4(a and c) shows the Fourier filtered images of the CNBI and CKBI powder samples, respectively.

An analysis of these images exhibits an almost equal inter-planar spacing (d) of approximately 3.52 Å and 3.53 Å, respectively, and is in agreement with the XRD values. The selected area electron diffraction (SAED) patterns of both the samples were recorded and are shown in Fig. 4(b and d). Both the images exhibit circular ring patterns, which reveals the poly-crystalline nature of the samples. The d values for both the CNBI and CKBI samples were calculated from the SAED patterns and were found to be ~3.47 Å, and 3.53 Å, respectively. The observed small difference between the inter-planar spacing shown in Fig. 4(c and d) could be attributed to the error that occurred while analysing the SAED data. In order to evaluate the absorption edge, UV-visible absorption measurements were performed. Fig. 5(a) shows the absorption spectra of the as synthesized films of the CNBI and CKBI samples. The results reveal that the CKBI perovskite sample shows maximum

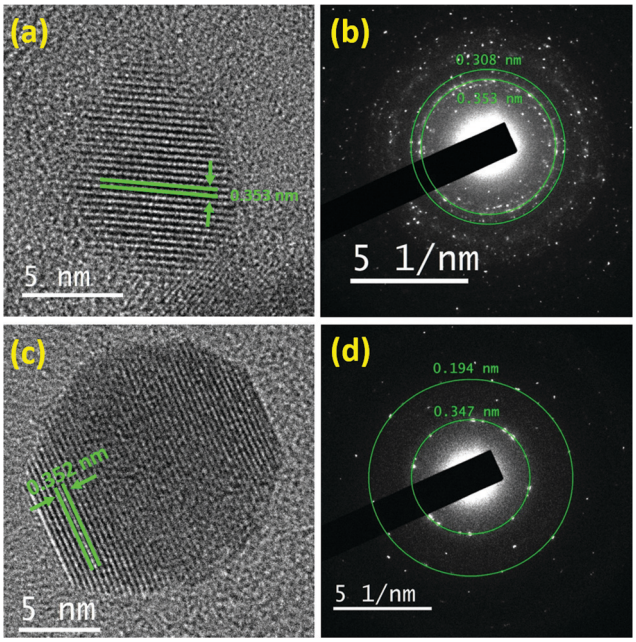

Fig. 4 (a and c) Fourier filtered high resolution transmission electron microscope (HRTEM) images of the CNBI and CKBI samples. (b and d) SAED patterns recorded from the CNBI and CKBI samples, respectively.

absorption in the 550 to 650 nm wavelength range, whereas the absorption maxima of the CNBI sample is a little red-shifted (580 to 670 nm). We further analysed these absorption spectra and converted them into Tauc plots using the Tauc relation, which reveals the optical band gap of CNBI and CKBI thin films ~1.94 and 1.98 eV, respectively (Fig. 5(b)).

Temperature-dependent PL study

Fig. 6 summarizes the temperature-dependent emission characteristics of both the perovskite films. The PL spectra of the CNBI and CKBI samples are shown in Fig. 6(a) and (b), respectively, where each spectrum shows a strong PL peak centered in the visible region. From the plots, it is observed that with increasing temperature from 77 K several changes in the emission profile appear including changes in the intensity, peak position, and line-width. Thermal dissociation of an exciton may be a possible reason for the suppression of radiative recombination (PL emission) with increasing temperature, and may also significantly enhance the electron–phonon temperature as has been found in other conventional semiconductors.[34,36–39] In order to investigate these changes in PL emission characteristics with temperature-variation, we de-convoluted each PL spectrum into Gaussian peaks using commercial software (PeakFit). Fig. 6(c) and (d) demonstrate sample images of the de-convoluted PL spectra of CNBI and CKBI samples, respectively, both recorded at 77 K. Here, it is worthwhile to mention that while de-convoluting, we corrected each peak position by adopting the approach suggested by Bebb and Williams,[40] followed by baseline correction to remove the background signal. In panels (c) and (d) the black traces represent raw data, and red traces the theoretical fitted data. The fitting of the PL spectrum shown in Fig. 6(c) shows that the raw data is best fitted with a strong peak centered around ~649 nm (1.910 eV) followed by an additional weak peak at ~720 nm. A similar trend is observed from the fitting of the PL spectrum of the CKBI sample shown in panel (d), where the major peak is centred at ~645 nm (1.9225 eV) with an additional peak at ~720 nm, at the same peak position as of CNBI. We mark these intense peaks as peak P_1 (1.910 eV), and peak P_2 (1.9225 eV), respectively. In general, trap emissions in semiconductors show temperature-dependent localization behavior, *i.e.* strongly localize at low temperatures and disappear at high temperatures (even below room temperature).[34] However, in this study, neither peak P_1 nor peak P_2 show any temperature-dependent localization behavior, thus omitting any possibility of the emergence of these lines from trap emissions. Additionally, a close match of these lines with the absorption edge at 1.94 and 1.98 eV, respectively, further confirms the emission not from the trap centers but from the excitonic transitions.

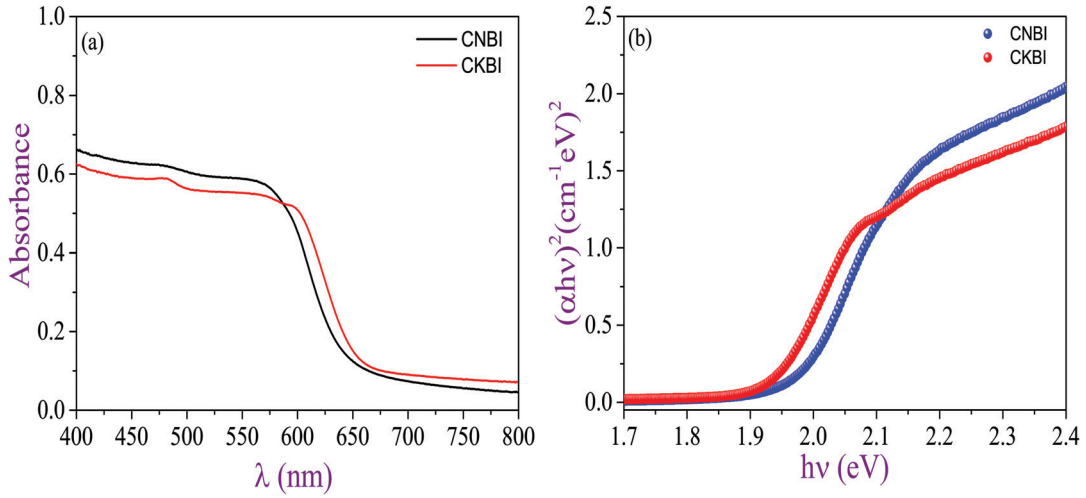

Fig. 5 (a) Room temperature absorption spectra of the CNBI and CKBI perovskite films. (b) Tauc plots of the CNBI and CKBI perovskite films.

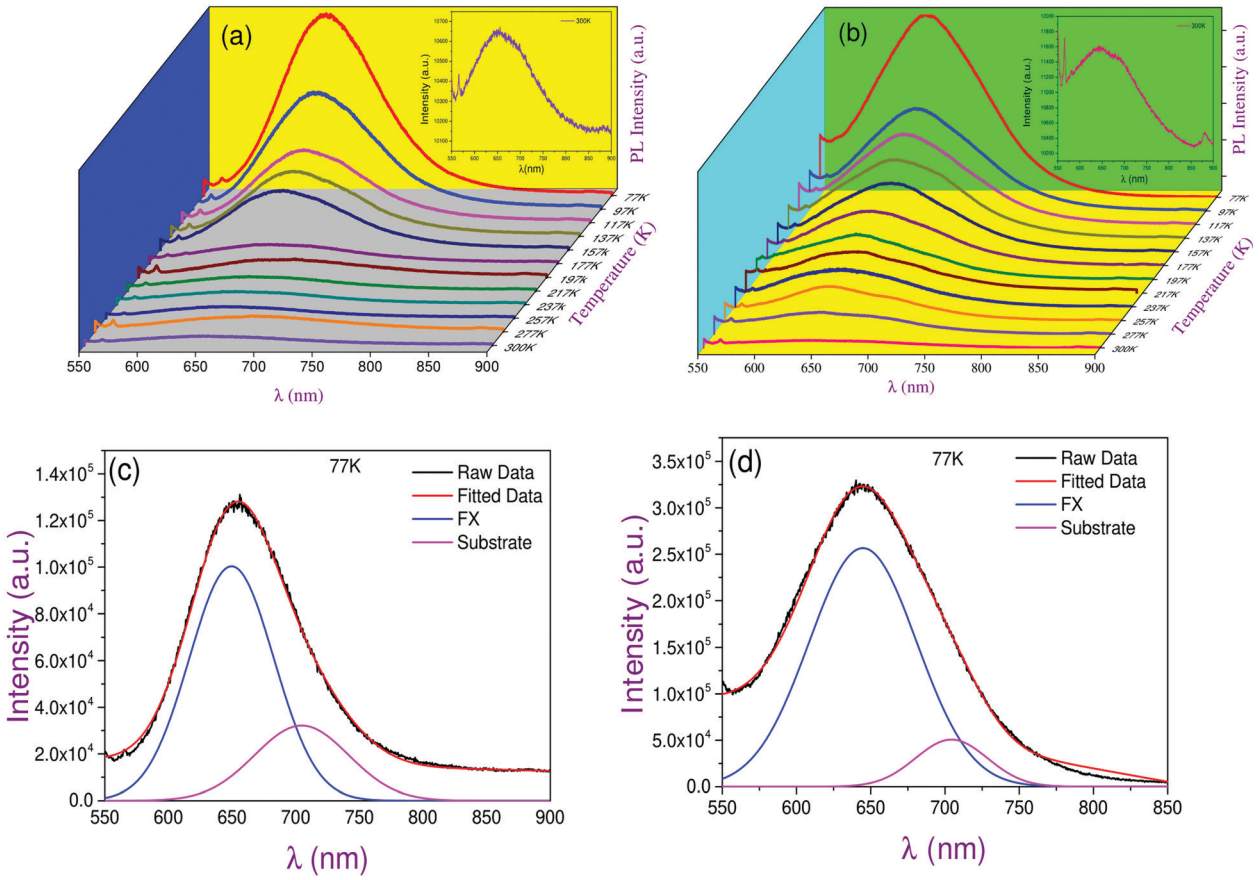

Fig. 6 (a and b) Temperature-dependent PL spectra of samples CNBI and CKBI, respectively. Inset of (a) and (b) demonstrate the room temperature PL spectra of the respective samples. (c and d) Plots of deconvoluted PL spectra of CNBI and CKBI samples recorded at 77 K, respectively.

These excitonic transitions include both the possibility of an exciton bound to a very shallow trap state, and free-exciton (FX) recombination. Generally, at low temperatures, the emission lines originating from an exciton bound to a very shallow trap state show no thermal broadening due to the lack of kinetic energy.[35] By considering all these facts we attribute peaks P_1 and P_2 to the FX recombination. Here, it is worthwhile mentioning that before recording the PL spectra of the perovskite samples, we also recorded the PL spectrum of the bare substrate, which shows a weak line originating at 720 nm.[17] Hence, we attribute the additional peak emerging in the de-convoluted PL spectra to the FTO coated glass substrate. Taking these low-temperature PL spectra as a reference for the respective samples, we de-convoluted the PL spectra of the entire temperature range and observe that temperature variation strongly affects the emission characteristics of both CNBI and CKBI films, as evident in panels (a) and (b). Post de-convolution, we extracted the integrated intensity (area under the curve) of the FX peak of both the films, and plotted it as a function of temperature in Fig. 7(a), where the blue and green dotted curves represent the experimentally obtained integrated intensity of peaks P_1 and P_2. Here, we observe that the integrated intensity of the FX peaks of both the samples exhibit distinct temperature-dependent quenching behavior. Noticeably, from the plots it can be easily seen that the temperature-dependent quenching in the integrated intensity of peak P_1 in CNBI is more rapid beyond a temperature of 157 K compared to that of peak P_2 in CKBI.

Additionally, the plots also show that the population of radiative transitions (PL yield) at low temperature (77 K) is almost double for CKBI than for CNBI and is significant up to 160 K. The population of radiative recombination depends on several factors including the quality of the film, defect densities, the concentration of non-radiative transitions, temporary storage of charge carriers, dark-fraction losses, band-edge losses, electron–phonon interaction, and dissociation of an exciton.[41] In the present case, as we didn't observe any line originating from the defect centers, which omits the possibility of a non-radiative carrier transfer to the defect centers.[34] However, the factors mentioned above may also play a small role, but the high activation energy (exciton binding energy, calculated in the next section) suggests the dissociation of free excitons into the continuum states is the most possible mechanism among others for the quenching of the FX intensity.[17] The observed thermal quenching of the FX emissions could be well described with the familiar Arrhenius equation:[42]

$$I(T) = \frac{I_0}{1 + A\ \exp(-E_a/k_B T)} \quad (3)$$

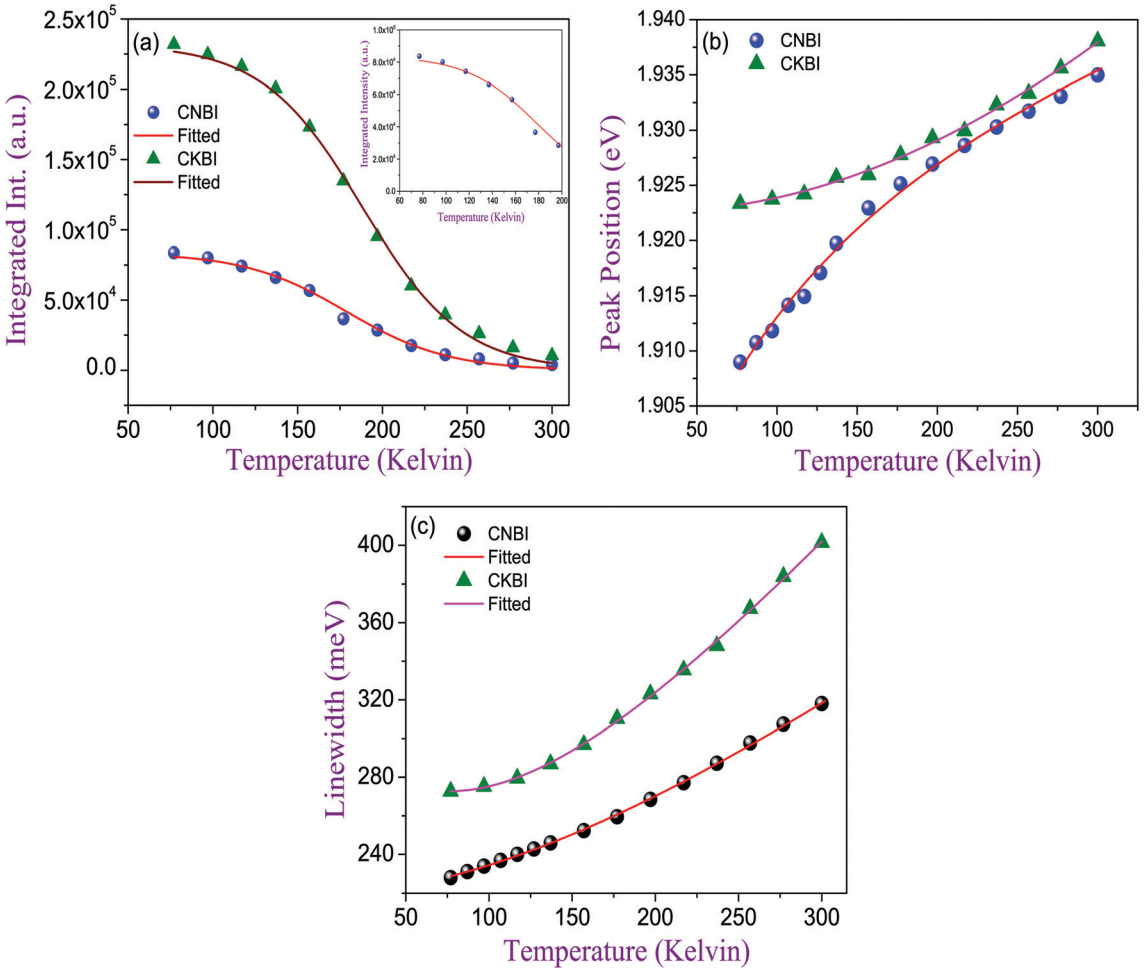

Fig. 7 (a) The blue and green dotted curves plot the integrated intensity of the FX peaks of samples CNBI and CKBI, respectively, and the solid lines show theoretical fits. The inset displays variation in the integrated intensity of peak P_1 in the temperature range between 77 K and 200 K. (b) Temperature-dependent variation in the energy of FX peaks P_1 and P_2, and the solid lines are a guide to the eyes. (c) Temperature-dependent line broadening of the FX peaks obtained from de-convolution of the PL spectra of CNBI and CKBI films.

where I_0 is the zero temperature intensity, E_a is the activation energy of nonradiative transitions or the exciton dissociation process, k_B is the Boltzmann constant and A is a normalization constant. Considering this equation we estimated the value of E_a for both peaks P_1 and P_2, as 36.5 ± 0.9 meV and 38.7 ± 1.2 meV, respectively, from which a difference of ~2.2 meV significantly supports our argument that exciton dissociation is responsible for a low PL yield of the CNBI sample compared to CKBI. The photophysical processes not only affect the recombination but also have an impact on the emission energy. Fig. 7(b) shows that both peaks P_1 and P_2 show a blue-shift with increasing temperature. Generally, in conventional semiconductors, the FX peak shows a red-shift with increasing temperature due to both the electron–phonon interaction and the lattice dilation.[34,43–45] However, in the literature, a blue-shift has been reported in perovskites. In this series, a report by Lee *et al.*[17] attributed this blue-shift to the widening of the valence band maxima (VBM) and conduction band minima (CBM), where both the VBM and CBM of lead halide perovskites (ABX_3) are formed by $B_{ns}X_{mp}$ antibonding orbitals and $B_{np}X_{ms}$ antibonding orbitals, respectively. Reports by Ghosh *et al.*,[46] Kumar *et al.*[47] and Davies *et al.*[48] suggested that the blue-shift in perovskites arises from the two types of emissions *i.e.* excitonic and free-charge carrier recombination whose relative contributions change with temperature.

In addition to this, the literature also claims that the contribution of the electron–phonon interaction is negligible, and the emphatic contribution of lattice thermal expansion with a positive temperature coefficient leads to a widening of the bandgap.[49] However, the underlying physics behind this blue-shift of the FX peak with increasing temperature is debatable and detailed theoretical and experimental investigations are strongly required for a better understanding of its origin. In context to caesium based perovskites, the band gap calculation of $CsSnBr_3$ also shows that the VBM is formed between the p orbit of Br and the s orbit of Sn,[50,51] and we hypothesized a similar behavior for our CNBI and CKBI films. However, detailed band calculations and a study of the relative contributions from excitonic and free-charge carrier recombination of these perovskites are needed and remain an open problem, which may provide better understanding about the fundamental mechanism behind this blue-shift and support for

our hypothesis. Fig. 7(c) summarizes the temperature-dependent line broadening (FWHM) of peaks P_1 and P_2, where the dotted curves represent the experimental data. From the plots we can see that the FWHM of both peaks P_1 and P_2 broaden monotonously with increasing temperature. For comparison, we have listed the observed line broadening along with other reported perovskites in Table 1. From the table it is seen that the line broadening in both the CNBI and CKBI samples is larger than for the lead based perovskites, and we attribute this to the inhomogeneous broadening of the emission due to size dispersion, surface roughness, and phonon coupling as the dominant spectral broadening mechanism.[53]

The temperature dependent line broadening observed in Fig. 7(c) can be explained by the following model:[34,52]

$$\Gamma(T) = \Gamma_0 + \gamma_{ph} T + \left[\frac{\Gamma_{LO}}{\exp(\hbar\omega_{LO}/K_B T) - 1}\right] \quad (4)$$

where Γ_0 is the inhomogeneous broadening contribution, γ_{ph} is the exciton–acoustic phonon interaction strength, Γ_{LO} is the carrier-LO phonon coupling coefficient, and $\hbar\omega_{LO}$ is the LO phonon energy. The solid line in Fig. 7(c) represents fitting of the above equation. From the fitting it is observed that both the acoustic and longitudinal optical phonon scattering contribute to the line broadening, and the extracted parameters are listed in Table 2. The obtained fitting parameters indicate that the exciton–phonon interaction (both acoustic and LO) is stronger in CNBI compared to in CKBI, which may also affect the population rate as seen in the integrated intensity plots.

Table 2 Extracted fitting parameters for line broadening of CNBI and CKBI perovskite films, and some other perovskites

Sample	Γ_0 (meV)	γ_{ph} (meV K^{-1})	Γ_{LO} (meV)	$\hbar\omega_{LO}$ (meV)	Ref.
Cs_2NaBiI_6	32.7	0.94	190.2	88	This work
Cs_2KBiI_6	35.3	0.47	199.4	78	This work
$FAPbI_3$	19		40	11.5	54
$FAPbBr_3$	20		61	15.3	54
$MAPbI_3$	26		40	11.5	54
$MAPbBr_3$	32		58	15.3	54
$(PEA)_2Pb_1I_4$	30		70	29	57
$(PEA)_2(CH_3NH_3)_2[Pb_3I_{10}]$	79		231	49	57
$CsPbBr_3$	37.20		13.78	45.02	58
$CsPbBr_{2.25}Cl_{0.75}$	28.49		20.28	65.72	58

Third-order optical nonlinear measurements

The measurements of third-order nonlinear coefficients (*i.e.* n_2 and β) were obtained using a single excitation beam technique (Z-Scan). This technique is used to determine the sign and values of n_2 and β directly. In Z-Scan, the variation in the transmission of the excitation laser is measured in the far-field as the sample is translated along the direction of propagation of the focused beam. This results in alteration of the phase-front as well as the power in the optical beam, recorded by a suitable detector through an aperture, which could be a partially closed aperture (CA)-configuration or it could be completely open aperture (OA)-configuration. The nonlinear measurements were performed with a beam energy density ~150 GW cm^{-2} at a pulse repetition rate of 1 kHz. The measured CA and OA transmissions are shown in Fig. 8 (black dotted-curves). In order to rule out the contribution from the substrate in our NLO measurements, we obtained the Z-scan transmission traces for the FTO coated glass substrate in both CA and OA configurations at identical pump powers and subtracted them from the actual measurements of the perovskite films. It is worthwhile mentioning that the alteration of pump power from 50–150 GW cm^{-2} resulted in a very small change in the normalized transmission for both the CA and OA configurations and the transmission profile remained unchanged. The CA transmission could contain a contribution from nonlinear absorption (if significant) in addition to the signature of nonlinear refraction. The measured CA normalized transmission for CNBI and CKBI films are shown Fig. 8(a) and (b), respectively. It is apparent that both the samples exhibit a pre-focal maximum (peak) followed by a post-focal minimum (valley) which is a typical signature of the self-defocusing effect or alternately, the nonlinear refractive index (n_2) bears a negative sign.[60] In order to estimate the values of nonlinear coefficients, the normalized transmittance is fitted with eqn (5).[29,59]

$$T(z, \Delta\phi_0) = 1 - \frac{4\Delta\phi_0 x}{(x^2+9)(x^2+1)} - \frac{2(x^2+3)\Delta\Psi_0}{(x^2+9)(x^2+1)} \quad (5)$$

where, $x = z/z_0$ is the relative sample position, $\Delta\phi_0 = kn_2 I_0 L_{eff}$ is the phase change due to nonlinear refraction, $\Delta\Psi_0 = \beta I_0 L_{eff}$ represents

Table 1 Comparison of the line width of CNBI and CKBI perovskite films with some other perovskites

Sample	Structure	λ (nm)	Temperature (K)	FWHM	Ref.
Cs_2NaBiI_6	Film	532	77–300	228–353 meV	This work
Cs_2KBiI_6	Film	532	77–300	273–400 meV	This work
$CsPbBr_3$	Quantum dots	1064	30–290	190–233 meV	17
$CsPb(Br/I)_3$	Quantum dots	1064	30–290	205–210 meV	17
$FAPbI_3$	Film	398	10–370	20–100 meV	54
$FAPbBr_3$	Film	398	10–370	20–210 meV	54
$MAPbI_3$	Film	398	10–370	20–120 meV	54
$MAPbBr_3$	Film	398	10–370	30–135 meV	54
$CsPbBr_3$	Nano-crystals	400	300–373	75–86 meV	16
$CsPbX_3$,(X = Cl, B, I)	Colloidal solution of nano-crystals	365	300	12–42 nm	15
$CsPb_xMn_{1-x}Cl_3$	Colloidal solution of quantum dots	340–380	423–463	12–80 nm	55
$MAPbBr_3$	Film	405	78–320	50–170 meV	56
$MAPbI_3$	Film	405	78–320	45–85 meV	56

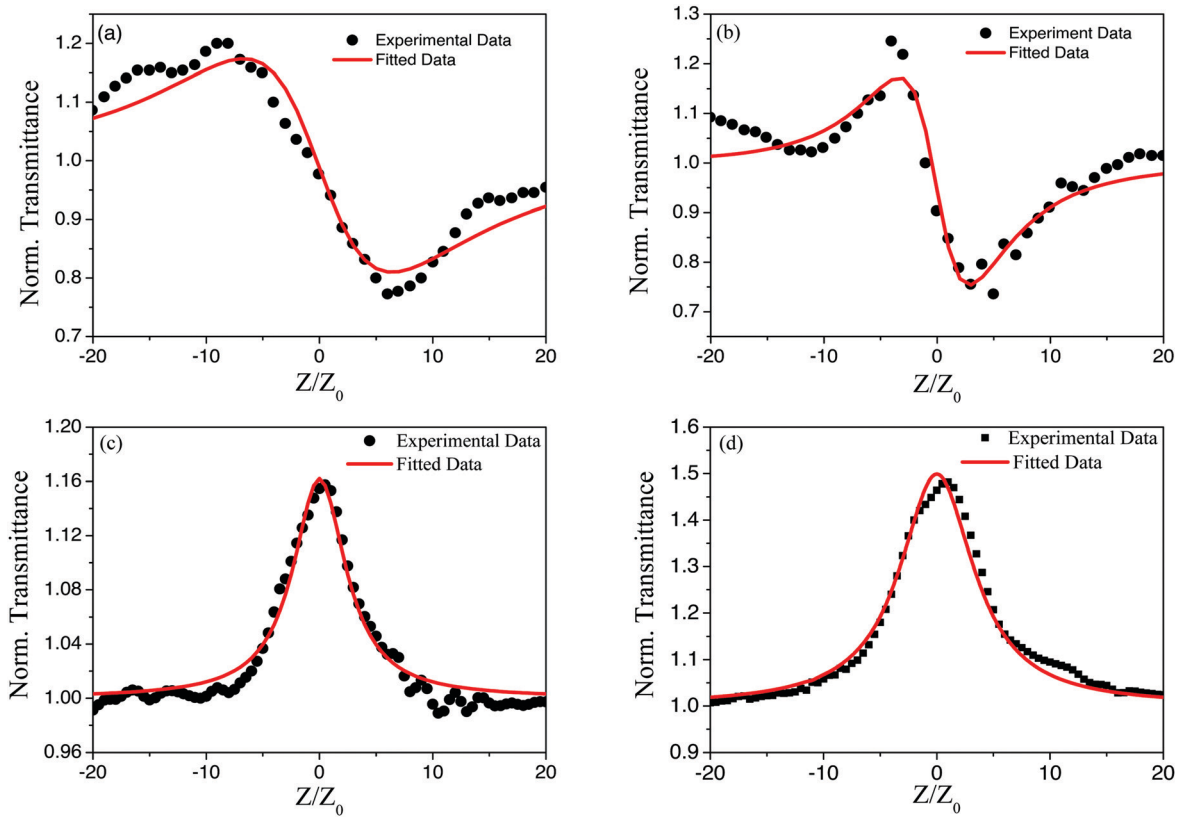

Fig. 8 (a and c) Z-scan traces of the CNBI film recorded in CA and OA configurations, respectively. Similarly, traces of the CKBI film recorded in CA and OA configurations are plotted in panels (b) and (d) (black dotted-curves), respectively.

the phase changes due to nonlinear absorption, I_0 is the on-axis intensity of the laser beam at the focal point, and L_{eff} is the effective sample thickness. A prior knowledge of β assists in obtaining a better fit to CA transmittance and hence, a more accurate estimation of n_2. Therefore, the OA transmittance is measured for both the CNBI and CKBI samples which exhibit a peak at the focal point and are presented in panels (c) and (d) of Fig. 8. The appearance of this transmittance peak at the focal point is a signature of saturable absorption (SA) behavior. For an OA configuration, the normalized transmittance is essentially dictated by eqn (6):[61]

$$T(z, s = 1) = 1 - \frac{\beta I_0 L_{\text{eff}}}{2^{3/2}(1 + x^2)} \quad (6)$$

It is important to appreciate that eqn (5) and (6) are derived using a Gaussian beam decomposition method and it assumes the incident laser beam to have $M^2 = 1$. Any scattering mechanism which distorts the Gaussian beam wave front would essentially result in an error in estimation of n_2 as well as β.[4] The non-uniformity in the CNBI film tends to distort the beam, which adversely affects the fit in panel (c) in comparison to that of CKBI in panel (d). From the fitting, the obtained NLO parameters are summarised in Table 3. In addition to this, the reported NLO coefficients for a few perovskites are also tabulated. A comparison elucidates that β for CNBI and CKBI is less with respect to the Pb based perovskites. The usually high β value reported in ref. 4 and 62 is essentially due to the significant contribution from free carrier and two-photon absorption mechanisms. Similarly, our n_2 values are less than the Pb based perovskites. In general, the third-order ($\chi^{(3)}$) nonlinear optical processes could essentially be due to resonant or non-resonant interactions of the medium with coherent EM-radiation. The thermo-optic manifestations, which are mediated through phonon-photon interaction usually fall into the non-resonant category and have negligible contribution when the excitation sub-picosecond laser has a low repetition rate (a few kHz). The resonant intensity nonlinearity, on the other hand, are slow and attributed to real transitions. It is worth mentioning that the perovskites typically exhibit absorption bands (due to linear absorption) in the visible band of the EM-spectrum. Therefore, in order to avoid any resonant (linear as well as nonlinear) optical effects, the nonlinear absorption measurements were carried out at near-infrared (at 1030 nm wavelength). Consequently, the optical nonlinear response observed in the CNBI and CKBI films is essentially dominated by simultaneous absorption of multiple photons through virtual transitions. This non-resonant multi-photon absorption process could be attributed to the bound charges, which lead to a significant dipole moment change upon ultra-short pulsed excitation. Additionally, the SA behavior in both the CNBI and CKBI films is a signature of the Pauli blocking effect, which comes into effect when the excitation intensity is high. In this case, the intensity is $\sim$150 GW cm^{-2} at the focus, which leads

Table 3 Summary of the NLO parameters of CNBI and CKBI perovskites along with some perovskites/other materials reported in the literature

Sample	Structure	n_2 (cm^2 W^{-1})	β (cm W^{-1})	λ (nm)	Pulse duration	Ref.
Cs_2NaBiI_6	Film	$-1.06 \pm 0.081 \times 10^{-14}$	$-6.23 \pm 3.9 \times 10^{-12}$	1030	370 fs	This work
Cs_2KBiI_6	Film	$-1.34 \pm 0.20 \times 10^{-14}$	$-1.14 \pm 0.27 \times 10^{-12}$	1030	370 fs	This work
$CH_3NH_3PbI_3$	Film	2.1×10^{-12}	-0.5×10^{-6}	1028	200 fs	4
$CsPbBr_3$	Quantum dots		8.5×10^{-11}	800	100 fs	22
$(CH_3(CH_2)_3NH_3)_2(CH_3NH_3)_3Pb_4I_{13}$	Powder	9.6×10^{-11}	2.19×10^{-8}	1064	30 ps	62
$CsPbI_3$	Colloidal solution	$3–8 \times 10^{-13}$	$3–5\times 10^{-10}$	1064	1 ns	63
$MAPb_{0.75}Sn_{0.25}I_3$	Film		1.15×10^{-3}	1535	400 fs	64
$(Cs_{0.06}FA_{0.79}MA_{0.15})$ $Pb(I_{0.85}Br_{0.15})_3$	Film	1×10^{-11}	$(100–0.43) \times 10^{-6}$	790	50 fs	65
$(PEA)_2PbI_4$	Film		211.5×10^{-6}	800	100 fs	66
$(BA)_2MAPb_2I_7/(BA)_2PbI_4$	Film		44.0×10^{-6}	800	100 fs	67
$(CH_3(CH_2)_3NH_3)_2(CH_3NH_3)$ Pb_2I_7	Quantum dots		720×10^{-9}	532		68
$(BPSCA)_2MAPb_2I_7$	Film	1.2×10^{-13}	$11.25 \pm 2.0 \times 10^{-9}$	800	100 fs	69
$CsPbCl_3$	Nanocrystal		7.91×10^{-13}	630	100 fs	70
$CsPbCl_3$	Quantum dots		1.36×10^{-11}	787	100 fs	71
$CsPbI_3$	Quantum dots		1.54×10^{-11}	787		71
$MAPbI_3$	Film		-4.6×10^{-16}	1560	2.8 ps	72
$MAPbI_3$	Film		-152×10^{-6}	532	40 ps	73
$MAPbI_3$	Nanosheet		-1.934×10^{-6}	800	140 fs	74
$MAPbI_3$	Single crystal		-1.934×10^{-6}	1064	30 ps	75
ZnO	Nanorods	2.1×10^{-10}	3.5×10^{-5}	532	0.7 ns	29
Silicon	Crystalline	5.41×10^{-10}	3.26×10^{-8}	1064	11.5 ns	76
GaAs	Film	-9.4×10^{1}	3.25×10^{-13}	1550		73
CdTe	Quantum dots	2.5×10^{-12}	1.5×10^{-7}	800		77
Bi_2Te_3	Nanostructures	9.402×10^{-13}		532	4 ns	78

to accumulation of bound charges in the near-bottom levels of the higher valence band. This tends to adversely affect the two-photon (or multi-photon) absorption probability and subsequently, the SA signature at high laser intensity.[4]

Conclusion

Given the challenges of finding air-stable, non-toxic alternatives to the lead halide perovskites, it is highly encouraging to find double perovskites with band gaps that are comparable to their lead based perovskite analogs. In summary, lead-free and eco-friendly CNBI and CKBI perovskite films were deposited on FTO coated glass substrates using a drop cast method. The XRD patterns confirm the synthesis of double perovskites. The optical band gaps of the CNBI and CKBI perovskites were estimated to be 1.94 and 1.98 eV, respectively, from their UV-Vis absorption spectra. The temperature dependent excitonic emission characteristics and room temperature NLO properties of both the CNBI and CKBI films were investigated under ambient conditions using PL spectroscopy and Z-scan techniques respectively. The PL spectra of the CNBI and CKBI samples showed temperature-dependent excitonic emission behavior, where thermal quenching of the FX emission along with temperature-dependent line broadening and a blue-shift of the FX peaks with increasing temperature were observed. We attribute this thermal quenching of the FX peaks to dissociation of excitons with increasing temperature. The temperature-dependent line broadening of the FX peaks in both the CNBI and CKBI samples fits well with the model incorporating inhomogeneous broadening, exciton-acoustic phonon interaction strength and exciton-LO phonon coupling. The blue-shift in the FX peaks may either arise due to widening of the band gap through slight changes in the potential energy in the VBM and CBM, or the change of relative contributions from the excitonic and free-charge carrier recombination with temperature. However, detailed theoretical band calculations and investigation of the relative contributions from these two types of emissions with the temperature of these perovskites are needed, which may provide a better understanding of the fundamental mechanism behind the blue-shift. In NLO measurements, the self-defocusing effect (negative n_2 value) is evident from both the CNBI and CKBI samples. The observed SA characteristics of the samples are attributed to the unavailability of unoccupied states for the nonlinear optical transitions to take place. The apparent excellent excitonic emission characteristics and NLO properties of the CNBI and CKBI perovskite films in ambient conditions indicate their applicability for designing cost-effective and lead-free optoelectronic and NLO applications.

Conflicts of interest

There are no conflicts to declare.

Acknowledgements

The authors thank the Indian Institute of Technology, Kanpur, UP, India, and the National Institute of Science Education and Research, Bhubaneswar, HBNI, India for use of their facilities. A. S. is also thankful to Dr Dhananjay Dey for his help during the UV-Vis measurements. Avanendra Singh acknowledges financial support from DST, SERB, and the Government of India for the grant PDF/2018/002981.

References

1 Z.-K. Tan, R. S. Moghaddam, M. L. Lai, P. Docampo, R. Higler, F. Deschler, M. Price, A. Sadhanala, L. M. Pazos and D. Credgington, *et al.*, Bright Light-Emitting Diodes Based on Organometal Halide Perovskite, *Nat. Nanotechnol.*, 2014, **9**, 687–692.

2 G. Xing, N. Mathews, S. S. Lim, N. Yantara, X. Liu, D. Sabba, M. Grätzel, S. Mhaisalkar and T. C. Sum, Low-Temperature Solution-Processed Wavelength-Tunable Perovskites for Lasing, *Nat. Mater.*, 2014, **13**, 476–480.

3 D. Shi, V. Adinolfi, R. Comin, M. Yuan, E. Alarousu, A. Buin, Y. Chen, S. Hoogland, A. Rothenberger and K. Katsiev, *et al.*, Low Trap- State Density and Long Carrier Diffusion in Organolead Trihalide Perovskite Single Crystals, *Science*, 2015, **347**, 519–522.

4 B. S. Kalanoor, L. Gouda, R. Gottesman, S. Tirosh, E. Haltzi, A. Zaban and Y. R. Tischler, *ACS Photonics*, 2016, **3**, 361–370.

5 W. Shen, J. Chen, J. Wu, X. Li and H. Zeng, Nonlinear Optics in Lead Halide Perovskites: Mechanisms and Applications, *ACS Photonics*, 2021, **8**, 113–124.

6 X. Li, X. Gao, X. Zhang, X. Shen, M. Lu, J. Wu, Z. Shi, V. L. Colvin, J. Hu, X. Bai, W. W. Yu and Y. Zhang, Lead-Free Halide Perovskites for Light Emission: Recent Advances and Perspectives, *Adv. Sci.*, 2021, **8**, 2003334.

7 Z. Xiao, R. A. Kerner, L. Zhao, N. L. Tran, K. M. Lee, T.-W. Koh, G. D. Scholes and B. P. Rand, Efficient perovskite light-emitting diodes featuring nanometre-sized crystallites, *Nat. Photonics*, 2017, **11**, 108–115.

8 W. Xu, *et al.*, Rational molecular passivation for high-performance perovskite light-emitting diodes, *Nat. Photonics*, 2019, **13**, 418–424.

9 T. Matsushima, F. Bencheikh, T. Komino, M. R. Leyden, A. S. D. Sandanayaka, C. Qin and C. Adachi, High performance from extraordinarily thick organic light-emitting diodes, *Nature*, 2019, **572**, 502–506.

10 W. S. Yang, J. H. Noh, N. J. Jeon, Y. C. Kim, S. Ryu, J. Seo and S. I. Seok, High-Performance Photovoltaic Perovskite Layers Fabricated through Intramolecular Exchange, *Science*, 2015, **348**, 1234–1237.

11 H. Tan, A. Jain, O. Voznyy, X. Lan, F. P. G. de Arquer, J. Z. Fan, R. Quintero-Bermudez, M. Yuan, B. Zhang, Y. Zhao, F. Fan, P. Li, L. N. Quan, Y. Zhao, Z.-H. Lu, Z. Yang, S. Hoogland and E. H. Sargent, Efficient and stable solution-processed planar perovskite solar cells via contact passivation, *Science*, 2017, **355**, 722–726.

12 S. W. Eaton, M. Lai, N. A. Gibson, A. B. Wong, L. Dou, J. Ma, L.-W. Wang, S. R. Leone and P. Yang, Lasing in robust cesium lead halide perovskite nanowires, *Proc. Natl. Acad. Sci. U. S. A.*, 2016, **113**, 1993–1998.

13 Y. Wang, X. Li, J. Song, L. Xiao, H. Zeng and H. Sun, All-Inorganic Colloidal Perovskite Quantum Dots: A New Class of Lasing Materials with Favorable Characteristics, *Adv. Mater.*, 2015, **27**, 7101–7108.

14 M. G. Ehrenreich, Z. Zeng, S. Burger, M. R. Warren, M. W. Gaultois, J.-C. Tan and G. Kieslich, Mechanical properties of the ferroelectric metal-free perovskite [MDAB-CO](NH4)I3, *Chem. Commun.*, 2019, **55**, 3911–3914.

15 L. Protesescu, S. Yakunin, M. I. Bodnarchuk, F. Krieg, R. Caputo, C. H. Hendon, R. X. Yang, A. Walsh and M. V. Kovalenko, Nanocrystals of Cesium Lead Halide Perovskites (CsPbX3, X = Cl, Br, and I): Novel Optoelectronic Materials Showing Bright Emission with Wide Color Gamut, *Nano Lett.*, 2015, **15**, 3692–3696.

16 A. Swarnkar, R. Chulliyil, V. K. Ravi, M. Irfanullah, A. Chowdhury and A. Nag, Colloidal CsPbBr3 Perovskite Nanocrystals: Luminescence beyond Traditional Quantum Dots, *Angew. Chem., Int. Ed.*, 2015, **54**, 15424–15428.

17 S. M. Lee, C. J. Moon, H. Lim, Y. Lee, M. Y. Choi and J. Bang, Temperature-Dependent Photoluminescence of Cesium Lead Halide Perovskite Quantum Dots: Splitting of the Photoluminescence Peaks of CsPbBr3 and CsPb(Br/I)3 Quantum Dots at Low Temperature, *J. Phys. Chem. C*, 2017, **121**, 26054–26062.

18 J. Kang and L.-W. Wang, High Defect Tolerance in Lead Halide Perovskite CsPbBr3, *J. Phys. Chem. Lett.*, 2017, **8**, 489–493.

19 Y. Li, S. Guan, Y. Liu, G. Xu and B. Cai, Lasing properties of cesium lead halide perovskite nanowires fabricated by one-drop self-assembly and ion-exchange methods, *Opt. Express*, 2018, **26**, 33856–33864.

20 X. Wang, M. Shoaib, X. Wang, X. Zhang, M. He, Z. Luo, W. Zheng, H. Li, T. Yang, X. Zhu, L. Ma and A. Pan, High-Quality In-Plane Aligned CsPbX3 Perovskite Nanowire Lasers with Composition-Dependent Strong Exciton-Photon Coupling, *ACS Nano*, 2018, **12**, 6170–6178.

21 K. N. Krishnakanth, S. Seth, A. Samanta and S. V. Rao, Broadband femtosecond nonlinear optical properties of CsPbBr3 perovskite nanocrystals, *Opt. Lett.*, 2018, **43**, 603–606.

22 K. Wei, Z. Xu, R. Chen, X. Zheng, X. Cheng and T. Jiang, Temperature-dependent excitonic photoluminescence excited by two-photon absorption in perovskite CsPbBr3 quantum dots, *Opt. Lett.*, 2016, **41**, 3821–3824.

23 F. O. Saouma, C. C. Stoumpos, M. G. Kanatzidis, Y. S. Kim and J. I. Jang, Multiphoton Absorption order of CsPbBr3 as determined by wavelength-dependent nonlinear optical spectroscopy, *J. Phys. Chem. Lett.*, 2017, **8**(19), 4912–4917.

24 D. J. Clark, C. C. Stoumpos, F. O. Saouma, M. G. Kanatzidis and J. I. Jang, Polarization-selective three-photon absorption and subsequent photoluminescence in CsPbBr3 single crystal at room temperature, *Phys. Rev. B*, 2016, **93**, 195202.

25 B.-W. Park, B. Philippe, X. Zhang, H. Rensmo, G. Boschloo and E. M. J. Johansson, Bismuth Based Hybrid Perovskites A3Bi2I9 (A: Methylammonium or Cesium) for Solar Cell Application, *Adv. Mater.*, 2015, **27**, 6806–6813.

26 T. Miyasaka, A. Kulkarni, G. M. Kim, S. Oz and A. K. Jena, *Adv. Energy Mater.*, 2019, 1902500.

27 A. H. Slavney, T. Hu, A. M. Lindenberg and H. I. Karunadasa, *J. Am. Chem. Soc.*, 2016, **138**, 2138–2141.

28 A. Singh, *Extended and point defects assisted phenomena in ZnO nanorods*, Unpublished doctoral thesis, HBNI, Mumbai, and NISER, Bhubaneswar, India, 2018.
29 A. Singh, S. Kumar, R. Das and P. K. Sahoo, *RSC Adv.*, 2015, **5**, 88767.
30 C. Zhang, L. Gao, S. Teo, Z. Guo, Z. Xu, S. Zhao and T. Ma, *Sustainable Energy Fuels*, 2018, **2**, 2419.
31 P. Cheng, T. Wu, Y. Li, L. Jiang, W. Deng and K. Han, *et al.*, *New J. Chem.*, 2017, **41**, 9598.
32 M. Lyu, J. Yun, M. Cai, Y. Jiao, P. Bernhardt and M. Zhang, *et al.*, *Nano Res.*, 2016, **9**(3), 692.
33 X. Cui, K. Jiang, J. Huang, Q. Zhang, M. Su and L. Yang, *et al.*, Cupric bromide hybrid perovskite heterojunction solar cells, *Synth. Met.*, 2015, **209**, 247.
34 A. Singh, K. Senapati, B. Satpati and P. K. Sahoo, *Phys. Chem. Chem. Phys.*, 2017, **19**, 14012.
35 Y. Pelant and J. Valanta, *Luminescence Spectroscopy of Semi- conductors*, Oxford University Press, Oxford, UK, 2012.
36 B. Chon, J. Bang, J. Park, C. Jeong, J. H. Choi, J. B. Lee, T. Joo and S. Kim, Unique Temperature Dependence and Blinking Behavior of CdTe/CdSe (Core/Shell) Type-II Quantum Dots, *J. Phys. Chem. C*, 2011, **115**, 436–442.
37 J. Li, X. Yuan, P. Jing, J. Li, M. Wei, J. Hua, J. Zhao and L. Tian, Temperature-Dependent Photoluminescence of Inorganic Perovskite Nanocrystal Films, *RSC Adv.*, 2016, **6**, 78311–78316.
38 D. Valerini, A. CretiÌ, M. Lomascolo, L. Manna, R. Cingolani and M. Anni, Temperature Dependence of the Photoluminescence Properties of Colloidal CdSe/ZnS Core/Shell Quantum Dots Embedded in a Polystyrene Matrix, *Phys. Rev. B: Condens. Matter Mater. Phys.*, 2005, **71**, 235409.
39 G. Morello, M. De Giorgi, S. Kudera, L. Manna, R. Cingolani and M. Anni, Temperature and Size Dependence of Nonradiative Relaxation and Exciton-Phonon Coupling in Colloidal CdTe Quantum Dots, *J. Phys. Chem. C*, 2007, **111**, 5846–5849.
40 H. B. Bebb and E. W. Williams, in *Semiconductors and semimetals*, ed. R. K. Willardson and A. C. Beer, Academic, New York, 1972, vol. 8, p. 181.
41 S. J. W. Vonk, M. B. Fridriksson, S. O. M. Hinterding, M. J. J. Mangnus, T. P. van Swieten, F. C. Grozema, F. T. Rabouw and W. van der Stam, Trapping and Detrapping in Colloidal Perovskite Nanoplatelets: Elucidation and Prevention of Nonradiative Processes through Chemical Treatment, *J. Phys. Chem. C*, 2020, **124**, 8047–8054.
42 H. Diab, G. Trippe-Allard, F. Ledee, K. Jemli, C. Vilar, G. Bouchez, V. L. R. Jacques, A. Tejeda, J. Even, J.-S. Lauret, E. Deleporte and D. Garrot, Narrow Linewidth Excitonic Emission in Organic–Inorganic Lead Iodide Perovskite Single Crystals, *J. Phys. Chem. Lett.*, 2016, **7**, 5093–5100.
43 J. Wu, W. Walukiewicz, K. M. Yu, J. W. Ager, E. E. Haller, H. Lu, W. J. Schaff, Y. Saito and Y. Nanishi, Unusual Properties of the Fundamental Band Gap of InN, *Appl. Phys. Lett.*, 2002, **80**, 3967–3969.
44 Z. M. Gibbs, H. Kim, H. Wang, R. L. White, F. Drymiotis, M. Kaviany and G. J. Snyder, Temperature-Dependent Band Gap in PbX (X = S, Se, Te), *Appl. Phys. Lett.*, 2013, **103**, 262109.
45 P. Dey, J. Paul, J. Bylsma, D. Karaiskaj, J. M. Luther, M. C. Beard and A. H. Romero, Origin of the Temperature Dependence of the Band Gap of PbS and PbSe Quantum Dots, *Solid State Commun.*, 2013, **165**, 49–54.
46 S. Ghosh, Q. Shi, B. Pradhan, P. Kumar, Z. Wang, S. Acharya, S. Kalyan Pal, T. Pullerits and K. J. Karki, Phonon Coupling with Excitons and Free Carriers in Formamidinium Lead Bromide Perovskite Nanocrystals, *J. Phys. Chem. Lett.*, 2018, **9**, 4245–4250.
47 P. Kumar, Q. Shi and K. J. Karki, Enhanced Radiative Recombination of Excitons and Free Charges Due to Local Deformations in the Band Structure of MAPbBr3 Perovskite Crystals, *J. Phys. Chem. C*, 2019, **123**, 13444–13450.
48 C. L. Davies, M. R. Filip, J. B. Patel, T. W. Crothers, C. Verdi, A. D. Wright, R. L. Milot, F. Giustino, M. B. Johnston and L. M. Herz, Bimolecular recombination in methylammonium lead triiodide perovskite is an inverse absorption process, *Nat. Commun.*, 2018, **9**, 293–301.
49 C. L. Yu, Z. Chen, J. J. Wang, W. Pfenninger, N. Vockic, J. T. Kenney and K. Shum, Temperature Dependence of the Band Gap of Perovskite Semiconductor Compound CsSnI3, *J. Appl. Phys.*, 2011, **110**, 063526.
50 L. Huang and W. R. Lambrecht, *Phys. Rev. B: Condens. Matter Mater. Phys.*, 2013, **88**, 165203.
51 C. Yu, Z. Chen, J. J. Wang, W. Pfenninger, N. Vockic, J. T. Kenney and K. Shum, *J. Appl. Phys.*, 2011, **110**, 63526.
52 J. Lee, E. S. Koteles and M. O. Vassell, *Phys. Rev. B: Condens. Matter Mater. Phys.*, 1986, **33**, 5512.
53 C. Wehrenfennig, M. Liu, H. J. Snaith, M. B. Johnston and L. M. Herz, Homogeneous Emission Line Broadening in the Organo Lead Halide Perovskite CH3NH3PbI3_xClx, *J. Phys. Chem. Lett.*, 2014, **5**, 1300–1306.
54 A. D. Wright, C. Verdi, R. L. Milot, G. E. Eperon, M. A. Perez-Osorio, H. J. Snaith, F. Giustino, M. B. Johnston and L. M. Herz, Electron-phonon coupling in hybrid lead halide perovskites, *Nat. Commun.*, 2016, **7**, 11755.
55 H. Liu, Z. Wu, J. Shao, D. Yao, H. Gao, Y. Liu, W. Yu, H. Zhang and B. Yang, CsPbxMn1−xCl3 Perovskite Quantum Dots with High Mn Substitution Ratio, *ACS Nano*, 2017, **11**, 2239–2247.
56 Y. Liu, H. Lu, J. Niu, H. Zhang, S. Lou, C. Gao, Y. Zhan, X. Zhang, Q. Jin and L. Zheng, Temperature-dependent photoluminescence spectra and decay dynamics of MAPbBr3 and MAPbI3 thin films, *AIP Adv.*, 2018, **8**, 095108.
57 Y. Zhang, R. Wang, Y. Li, Z. Wang, S. Hu, X. Yan, Y. Zhai, C. Zhang and C. X. Sheng, Optical Properties of Two-Dimensional Perovskite Films of (C6H5C2H4NH3)2[PbI4] and (C6H5C2H4NH3)2(CH3NH3)2[Pb3I10], *J. Phys. Chem. Lett.*, 2019, **10**, 13–19.
58 Y. Song, X. Zhang, L. Li, Z. Mo, J. Xu, S. Yu, X. Liu and J. Zhang, Temperature-dependent photoluminescence of

cesium lead halide perovskite (CsPbX3, X = Br, Cl, I) quantum dots, *Mater. Res. Express*, 2019, **6**, 115064.

59 M. Yin, H. Li, S. H. Tang and W. Ji, *Appl. Phys. B: Lasers Opt.*, 2000, **70**, 587–591.

60 Y. Zhou, Y. Huang, X. Xu, Z. Fan, J. B. Khurgin and Q. Xiong, Nonlinear optical properties of halide perovskites and their applications, *Appl. Phys. Rev.*, 2020, **7**, 041313.

61 M. Sheik-Bahae, A. A. Said, T.-H. Wei, D. J. Hagan and E. W. Van Stryland, *IEEE J. Quantum Electron.*, 1990, **26**, 760–769.

62 F. O. Saouma, C. C. Stoumpos, J. Wong, M. G. Kanatzidis and J. I. Jang, *Nat. Commun.*, 2017, **8**, 742–749.

63 I. Suarez, M. Valles-Pelarda, A. F. Gualdron-Reyes, I. Mora-Sero, A. Ferrando, H. Michinel, J. R. Salgueiro and J. P. M. Pastor, *APL Mater.*, 2019, **7**, 041106.

64 Y. Xie, J. Fan, C. Liu, S. Chi, Z. Wang, H. Yu, H. Zhang, Y. Mai and J. Wang, Giant Two-Photon Absorption in Mixed Halide Perovskite $CH_3NH_3Pb_{0.75}Sn_{0.25}I_3$ Thin Films and Application to Photodetection at Optical Communication Wavelengths, *Adv. Opt. Mater.*, 2018, **6**, 1700819.

65 H. Syed, W. Kong, V. Mottamchetty, K. J. Lee, W. Yu, V. R. Soma, J. Yang and C. Guo, Giant Nonlinear Optical Response in Triple Cation Halide Mixed Perovskite Films, *Adv. Opt. Mater.*, 2020, **8**, 1901766.

66 W. Liu, J. Xing, J. Zhao, X. Wen, K. Wang, P. Lu and Q. Xiong, Giant Two-Photon Absorption and Its Saturation in 2D OrganicInorganic Perovskite, *Adv. Opt. Mater.*, 2017, **5**, 1601045.

67 J. Wang, Y. Mi, X. Gao, J. Li, J. Li, S. Lan, C. Fang, H. Shen, X. Wen, R. Chen, X. Liu, T. He and D. Li, Giant Nonlinear Optical Response in 2D Perovskite Heterostructures, *Adv. Opt. Mater.*, 2019, **7**, 1900398.

68 S. J. Varma, J. Cherusseri, J. Li, J. Kumar, E. Barrios and J. Thomas, Quantum dots of two-dimensional Ruddlesden-Popper organic-inorganic hybrid perovskite with high optical limiting properties, *AIP Adv.*, 2020, **10**, 045130.

69 C. K. Lim, M. Maldonado, R. Zalesny, R. Valiev, H. Agren, A. S. L. Gomes, J. Jiang, R. Pachter and P. N. Prasad, Interlayer Sensitized Linear and Nonlinear Photoluminescence of Quasi-2D Hybrid Perovskites Using Aggregation-Induced Enhanced Emission Active Organic Cation Layers, *Adv. Funct. Mater.*, 2020, **30**, 1909375.

70 J. Li, C. Ren, X. Qiu, X. Lin, R. Chen, C. Yin and T. He, Ultrafast optical nonlinearity of blue-emitting perovskite nanocrystals, *Photonics Res.*, 2018, **6**, 554.

71 S. Liu, G. Chen, Y. Huang, S. Lin, Y. Zhang, M. He, W. Xiang and X. Liang, Tunable fluorescence and optical nonlinearities of all inorganic colloidal cesium lead halide perovskite nanocrystals, *J. Alloys Compd.*, 2017, **724**, 889.

72 J. Yi, L. Miao, J. Li, W. Hu, C. Zhao and S. Wen, Third-order nonlinear optical response of CH3NH3PbI3 perovskite in the midinfrared regime, *Opt. Mater. Express*, 2017, **7**, 3894.

73 R. Zhang, J. Fan, X. Zhang, H. Yu, H. Zhang, Y. Mai, T. Xu, J. Wang and H. J. Snaith, Nonlinear Optical Response of Organic- Inorganic Halide Perovskites, *ACS Photonics*, 2016, **3**, 371.

74 P. Li, Y. Chen, T. Yang, Z. Wang, H. Lin, Y. Xu, L. Li, H. Mu, B. N. Shivananju, Y. Zhang, Q. Zhang, A. Pan, S. Li, D. Tang, B. Jia, H. Zhang and Q. Bao, Two-Dimensional CH3NH3PbI3 Perovskite Nanosheets for Ultrafast Pulsed Fiber Lasers, *ACS Appl. Mater. Interfaces*, 2017, **9**, 12759.

75 F. O. Saouma, D. Y. Park, S. H. Kim, M. S. Jeong and J. I. Jang, Multiphoton Absorption Coefficients of Organic-Inorganic Lead Halide Perovskites CH3NH3PbX3 (X = Cl, Br, I) Single Crystals, *Chem. Mater.*, 2017, **29**, 6876.

76 K. Ogusu and K. Shinkawa, Optical nonlinearities in silicon for pulse durations of the order of nanoseconds at 1.06 m, *Opt. Express*, 2008, **16**, 14780.

77 W. G. Lu, C. Chen, D. Han, L. Yao, J. Han, H. Zhong and Y. Wang, Nonlinear Optical Properties of Colloidal CH3NH3PbBr3 and CsPbBr3 Quantum Dots: A Comparison Study Using Z-Scan Technique, *Adv. Opt. Mater.*, 2016, **4**, 1732.

78 E. A. Hurtado-Aviles, M. Trejo-Valdez, J. A. Torres, C. J. Ramos-Torres, H. Martinez-Gutierrez and C. Torres-Torres, Photo-induced structured waves by nanostructured topological insulator Bi2Te3, *Opt. Laser Technol.*, 2021, **140**, 107015.

